Enhanced tuned mass damper using an inertial amplification mechanism

Enhanced Tuned Mass Damper using an Inertial Amplification Mechanism

Zhibao Cheng[a,*], Antonio Palermo[b], Zhifei Shi[a], Alessandro Marzani[b,*]

[a]*Institute of Smart Material and Structure, School of Civil Engineering, Beijing Jiaotong University, Beijing, 100044, China*
[b]*Department of Civil, Chemical, Environmental and Materials Engineering, University of Bologna, 40123, Italy*

Abstract

This paper proposes a novel inertial-amplification-mechanism (IAM) to enhance the vibration mitigation performance of the classical tuned-mass-damper (TMD). To this aim, the IAM is coupled to a standard TMD to form a so-called IAM-TMD. Analytical derivations are developed to extend the theory of the classical TMD to the IAM-TMD. Next, H_∞ and H_2 optimizations are performed and closed-form solutions for the optimal parameters of the IAM-TMD are obtained. Parametric studies are conducted to evaluate the influence of the geometrical configuration of the IAM system on the performance of the IAM-TMD. Finally, numerical simulations are performed to validate the efficiency of the IAM-TMD. In details, time history analyses of a structure without TMD, with TMD, and with IAM-TMD under harmonic and earthquake ground motions are computed and compared. Results show that when using the classical TMD, dynamic responses of the primary structure are suppressed, but the responses of the absorber are relatively large; conversely, when using the IAM-TMD, dynamic responses of both the primary structure and the absorber are mitigated at the same time.

Keywords: Tuned mass damper, Inertial amplification mechanism, H_∞ optimization, H_2 optimization, Vibrations mitigation

1. Introduction

Tuned mass dampers (TMDs) are widely used to mitigate vibrations of dynamic systems, like buildings or bridges, under wind loads, ground motions and

*Corresponding author

other dynamic loads. A TMD consists of a mass-spring-damping device attached to the main structure. With proper design, part of the vibration energy of the main structure is absorbed and dissipated by the attached mass-spring-damping system. As a result, the vibrations of the main structure are suppressed. In 1909, Frahm [1] introduced the concept of TMD as a mean to reduce the dynamic response of ships. In such work, the effect of damping was ignored. It was found that an undamped TMD is effective when the absorber's natural frequency is very close to the excitation frequency. Later works confirmed that the performance of an undamped TMD system deteriorates significantly when the excitation frequency deviates away from absorber's natural frequency. In order to eliminate this drawback, Ormondroyd and Den Hartog [2, 3] introduced the dashpot into the mass-spring TMD and derived closed-form expressions for optimal parameters of the absorber. After that, many analytical and numerical optimization methods have been developed to design TMDs in systems subjected to various types of excitation sources [4, 5, 6, 7, 8, 9]. Among the various, the fixed pointed theory [3, 4], also named as the H_∞ optimization method [10, 11, 12], has been proposed to estimate optimal TMD parameters for harmonic excitations, whereas the H_2 optimization method, generally based on the residue theorem [5, 13, 14] or on the linear control theory [10, 15, 12], has been successful developed for the case of white noise random excitation.

Over the past years, various works have been performed to investigate and expand the possible applications of TMDs in civil engineering. For example, it has been shown that the effectiveness of TMDs decreases as the input duration shortens. Therefore, their use is commonly discouraged against pulse-like ground motions occurring in near-field zones [16, 17]. Nonetheless, Matta [18] introduced a new optimization method as an alternative to the classical H_∞ optimization to show the possible applications of large-mass-ratio TMDs against impulsive loads. Similarly, Salvi et al. [19, 20] developed an optimization procedure for a hybrid TMD suitable to reduce the structural response under impulse loading. Several studies were instead devoted to account for uncertainties in the main structures, TMDs, as well as in the input excitations [21, 22, 23]. Lucchini et al. [23] proposed a method for the robust design of TMD systems considering the uncertainties in the properties of both the building and the input seismic excitation. In order to avoid possible mis-tuning due to the soil-structure interaction effects, Salvi et al. [24] investigated the effectiveness of an optimum TMD by embedding the soil-structure interaction effects within the dynamic and TMD optimization model. They found that optimum TMD configuration may change depending on the soil-structure interaction effects, especially for soft soils. Addi-

tionally, to achieve full control on the TMD motion, many semi-active and active TMDs were also developed as complementary or alternative with respect to passive TMDs [25, 26, 27].

Recently, a novel mechanical device, named *inerter*, has been proposed to mitigate the vibrations of different structures. In 2002 Smith [28] introduced the concept of the inerter by using the force-current analogy between mechanical and electrical network. After that, inerters were successfully proposed to improve the performance of machinery and components in the area of mechanical engineering, in particular for vehicle and train suspension systems [29, 30, 31, 32]. In a recent book [12], Chen and his co-workers presented a detailed description of the inerter and reported a comprehensive theoretical work on its dynamic properties and its application in vibration control systems. Hu and Chen [15] studied the proper arrangement of inerters in dynamic vibration absorbers, defining optimal inerter parameters via H_∞ and H_2 methods. To improve their performance, semi-active devices with changeable inertance were also considered [12, 33]. Similarly, using gear-ratio control systems, Brzeski et al. [34, 35] proposed a TMD that incorporates an inertance-changeable device.

Inspired by the successful application of inerters in mechanical engineering, several works proved their suitability in the context of civil engineering. In particular inerters have been proposed to improve the performance of conventional TMD and base isolation systems [36, 37]. For example, Ikago et al. [38] designed an inerter-like ball-screw mechanism to be used in a tuned viscous mass damper system for building systems, and tested its effectiveness for seismic excitation by shake table tests. Considering MDOF structures, Lazar et al. [39] analyzed the possibility of using a tuned inerter damper control system, connected between storeys, as an alternative to TMDs on the top of buildings. Similarly, Marian and Giaralis [40] proposed a passive vibration control configuration, namely the tuned-mass-damper-inerter, to suppress the seismic responses of structures. Later, the tuned-mass-damper-inerter was considered to suppress excessive wind-induced oscillations in tall buildings [41]. It was found that the tuned-mass-damper-inerter reduces peak top-floor acceleration more effectively than the TMD by utilizing smaller attached-mass. Furthermore, Giaralis and Taflanidis [42] investigated uncertainties in the hosting structure vs the performance of tuned-mass-damper-inerter. In an attempt to reduce the large displacements responses of the traditional seismic base isolation system, De Domenico et al. [43, 44] proposed an enhanced base-isolation system incorporating the inerter. Xu et al. [45] observed that the tuned-mass-damper-inerter system can reduce the vortex-induced vibration responses of bridge deck. Ma et al. [46] proposed a novel inerter-based

control system, namely a tuned-heave-plate-inerter, to suppress the excessive vibrations of offshore semi-submersible platforms. Their analytical results show that the tuned-heave-plate-inerter is more effective to mitigate the heave motion of semi-submersible platforms compared to the conventional methods, and the novel waterwheel inerter is capable of generating a large apparent mass by using a smaller waterwheel. Lu et al. [47] explored the potential of the viscous inertial mass damper to enhance the damping and mitigate the vibrations of stay cables in cable-stayed bridges. To provide a retrofit technology for in-service wind turbines, Zhang et al. [48] proposed the use of a lightweight energy dissipation device, the tuned parallel inerter mass system, for seismic response mitigation of the wind turbine tower. Zhao et al. [49] introduced a lightweight inerter system in the friction pendulum system to improve the seismic performances of base-isolated structures.

In the present work, a simple to realize inertial amplification mechanism (IAM) system is proposed to enhance the vibration mitigation performance of the classical TMD. Different from the widely-known flywheel-gear inerter [12], the mass amplification effect of the proposed system results from the geometrical amplification effect of a triangular-shape mechanical system. This amplification mechanism is very common in nature [50, 51, 52, 53, 54, 55] and has been exploited to enhance the performance of other mechanical systems, like enlarging the bandgap of phononic crystals [56, 57, 58], or amplifying the efficiency of energy harvesters [59, 60]. Here, by coupling the proposed IAM system with a classical TMD, a new inerter-based TMD, namely the IAM-TMD, is proposed to enhance the performance of traditional TMDs. In particular the addition of the IAM allows to suppress the responses of both the primary structure and the absorber. The theory of classical TMD is thus extended to investigate the dynamic properties of the IAM-TMD. To tackle the harmonic and white-noise random ground motion excitation, both the H_∞ and H_2 optimization are performed, from which closed-form solutions for the optimal IAM-TMD parameters are obtained. The superior performance of the IAM-TMD are related to the mass amplification effect of the inerter, indicated by using the 'inertance'. A larger inertance yields better vibration mitigation performance of the inerter. Therefore, our special attention is focused on the influences of the geometrical and physical parameters of the IAM system on its inertance and on the related performance of the IAM-TMD. Furthermore, with the aim to validate the efficiency of the proposed IAM-TMD, time history analyses are performed to compare the vibration mitigation performance of the classical TMD and the IAM-TMD. Numerical simulations show that, when the proposed IAM-TMD system is used, dynamic responses of both of the pri-

mary structure and the absorber are much smaller than those of the system with the classical TMD, even considering the entire mass of the IAM-TMD equal to the mass of the TMD.

This paper is organized as follows. Section 2 provides the basic concept of the proposed IAM system and the IAM-TMD system. Meanwhile, analytical derivations are also conducted in Section 2 to extend the theory of the traditional TMD system to the IAM-TMD system. Section 3 presents the H_∞ and the H_2 optimization procedures for harmonic and white-noise random ground motion inputs, respectively. Closed-form solutions for the optimal parameters of the IAM-TMD system are given in detail. Parametric analyses are performed to investigate the influences of the geometrical parameter and the mass distribution parameters of the IAM system on the performance of the IAM-TMD. Section 4 compares the time history results for three primary structures (without TMD, with TMD, and with IAM-TMD) under different kinds of ground motions, namely harmonic acceleration inputs, far-field as well as near-field earthquake acceleration inputs. Numerical results demonstrate the efficiency of the proposed IAM-TMD. Finally, some conclusions are drawn in Section 5.

2. Theoretical derivations

2.1. Proposed IAM

A schematic of the proposed IAM is shown in Figure 1a. The mechanism consists of four rigid bars, connected by hinges, and two lateral masses (m_a). The IAM undeformed configuration is defined by the angle θ, between the $x-$axis and the rigid bars. The top and bottom hinges can be connected to others mechanical elements in a dynamic system which operates in $x-$direction. Under the assumptions of small displacements along the $x-$axis, the displacements of the lateral masses are:

$$x_a = \frac{x_1 + x_2}{2}, \quad y_a = \pm\frac{x_2 - x_1}{2\tan\theta}. \tag{1}$$

To balance the inertial forces $f_{Ix} = m_a\ddot{x}_a$ and $f_{Iy} = m_a\ddot{y}_a$, the internal forces f_1 and f_2, as well as the overall reaction force F in Figure 1b are derived:

$$\begin{aligned} f_1 &= \tfrac{1}{2}\left(\tfrac{f_{Iy}}{\sin\theta} - \tfrac{f_{Ix}}{\cos\theta}\right), \quad f_2 = \tfrac{1}{2}\left(\tfrac{f_{Iy}}{\sin\theta} + \tfrac{f_{Ix}}{\cos\theta}\right), \\ F &= 2f_1\cos\theta = b(\ddot{x}_2 - \ddot{x}_1) + b^*(\ddot{x}_2 + \ddot{x}_1). \end{aligned} \tag{2}$$

in which $b = 0.5m_a\tan^{-2}\theta$ and $b^* = 0.5m_a$ are the inertial constants.

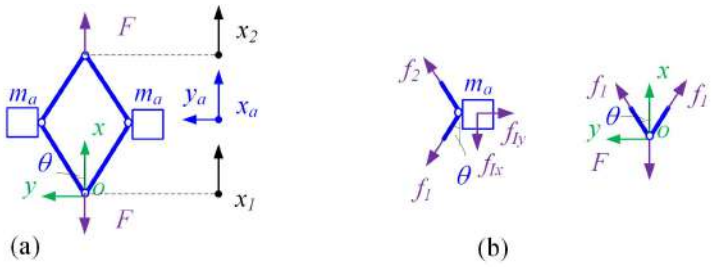

Figure 1: (a) IAM schematic diagram, (b) equilibrium configuration of the proposed IAM system.

As a result, the IAM can be seen as a one-dimensional mechanical system, which couples a classical inerter with a dead mass. For the classical inerter part, the inertial reaction force is proportional to the relative acceleration between the two terminals ($\ddot{x}_2 - \ddot{x}_1$), where the inertial constant b is governed by the geometrical configuration and lateral mass of the IAM. For the dead mass part, the inertial reaction force is proportional to the average acceleration between the two terminals ($(\ddot{x}_2 + \ddot{x}_1)/2$), where the inertial constant is only governed by the lateral mass.

2.2. Equation of motion of the IAM-TMD

The schematic of a primary structure equipped with an IAM-TMD is shown in Figure 2a. In this configuration, the IAM has its top hinge connected to the TMD and bottom one connected to the ground. The main structure is modeled as a SDOF system, with a stiffness k_s, a mass m_s, and a damping c_s [3, 5, 40]. Similarly, the stiffness, mass and damping coefficients of the IAM-TMD are respectively labelled as k_{id}, m_{id}, c_{id}, while the related parameters for the classical TMD (Figure 2b) as k_d, m_d, c_d. For the sake of comparison, the total mass of the IAM-TMD is set equal to that of the related classical TMD, i.e., $m_{id} + 2m_a = m_d$.

The equations of motion of the IAM-TMD-SDOF system can be written as:

$$\mathbf{M}\ddot{\mathbf{X}} + \mathbf{C}\dot{\mathbf{X}} + \mathbf{K}\mathbf{X} = -\mathbf{M_e}\mathbf{I}a_g(t), \tag{3}$$

where $\mathbf{X}=[x_s, x_{id}]^{\mathrm{T}}$ is the displacement vector retaining the relative displacements of the primary structure x_s and the absorber x_{id}, respectively, $\mathbf{I}=[1, 1]^{\mathrm{T}}$ is the index vector, and $\mathbf{K}$, $\mathbf{C}$, $\mathbf{M}$ and $\mathbf{M_e}$ are the stiffness, damping, mass and effective mass matrixes, respectively:

$$\mathbf{K} = \begin{bmatrix} k_s + k_{id} & -k_{id} \\ -k_{id} & k_{id} \end{bmatrix}, \mathbf{C} = \begin{bmatrix} c_s + c_{id} & -c_{id} \\ -c_{id} & c_{id} \end{bmatrix}, \tag{4}$$

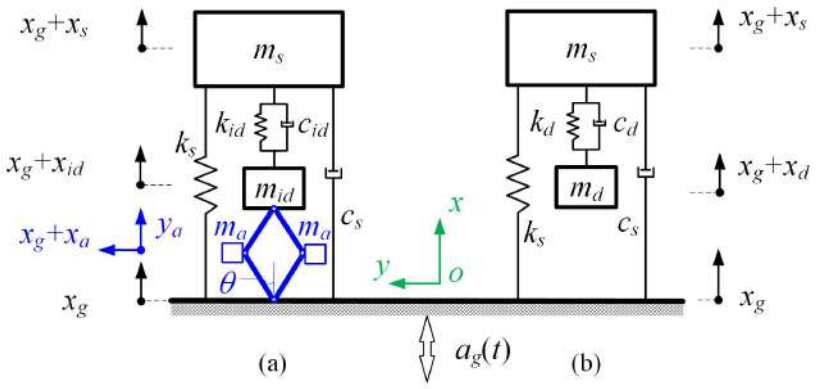

Figure 2: Theoretical model of the SDOF system with (a) the IAM-TMD and (b) the classical TMD.

$$\mathbf{M} = \begin{bmatrix} m_s & 0 \\ 0 & m_{id} + b_1 \end{bmatrix}, \mathbf{M_e} = \begin{bmatrix} m_s & 0 \\ 0 & m_{id} + m_a \end{bmatrix}. \tag{5}$$

in which $b_1 = b + b^* = 0.5m_a(1 + \tan^{-2}\theta)$.

2.3. Response to a harmonic ground motion

Considering a harmonic base excitation:

$$a_g(t) = a_g e^{i\omega t}, \tag{6}$$

where a_g is the acceleration amplitude of the ground motion, $i = \sqrt{-1}$ the imaginary unit, ω the angular frequency, the steady-state displacement response of the system can be obtained:

$$\mathbf{X} = \mathbf{X_0} e^{i\omega t}, \tag{7}$$

where $\mathbf{X_0} = [X_s, X_{id}]$ is the displacement amplitude vector:

$$\mathbf{X_0} = \frac{-\mathbf{M_e} \mathbf{I} a_g}{-\omega^2 \mathbf{M} + i\omega \mathbf{C} + \mathbf{K}}. \tag{8}$$

From Eq. (8), the transfer functions of the displacement responses of primary structure w.r.t. ground H_s and the relative displacement responses of absorber w.r.t. ground H_d can be obtained as:

$$H_s = \frac{X_s}{a_g}\omega_s^2 = \frac{R_s + iI_s}{P + iQ}, \tag{9}$$

$$H_d = \frac{X_{id} - X_s}{a_g}\omega_s^2 = \frac{R_d + iI_d}{P + iQ}, \tag{10}$$

in which:

$$\begin{aligned}
R_s = \;& (2\alpha - 1)(\mu - \alpha\mu + 1)f^2 + (\alpha\beta - 2\alpha + 1)r^2; \\
I_s = \;& -2fr(2\alpha - 1)(\mu - \mu\alpha + 1)\xi_{id}; \\
R_d = \;& \alpha(1 + r^2 - \beta r^2) - 1; \\
I_d = \;& 2r(1 - \alpha)\xi_s; \\
P = \;& (2\alpha - 1)(f^2 - r^2)(r^2 - 1) - \mu f^2 r^2 (2\alpha - 1)^2 \\
& -\alpha\beta r^2(\mu f^2(1 - 2\alpha) - r^2 + 1) \\
& +4fr^2(2\alpha - 1)\xi_{id}\xi_s; \\
Q = \;& -2r((2\alpha - 1)(f^2 - r^2) + \alpha\beta r^2)\xi_s \\
& +2fr(2\alpha - 1)((\mu - 2\alpha\mu + \alpha\beta\mu + 1)r^2 - 1)\xi_{id}.
\end{aligned} \tag{11}$$

and where the following normalized parameters have been introduced:

$$\begin{aligned}
Mass - ratio : \;& \mu = m_d/m_s; \\
Mass - distribution - ratio : \;& \alpha = m_a/m_d; \\
Inertance - ratio : \;& \beta = b_1/m_a; \\
Tuning - ratio : \;& f = \omega_{id}/\omega_s; \\
Forced - frequency - ratio : \;& r = \omega/\omega_s; \\
Damping - ratio : \;& \xi_s = c_s/(2\omega_s m_s); \\
& \xi_{id} = c_{id}/(2\omega_{id} m_{id}).
\end{aligned} \tag{12}$$

In Eq. (12) $\omega_s = \sqrt{k_s/m_s}$ and $\omega_{id} = \sqrt{k_{id}/m_{id}}$ are the eigen frequencies of the main structure and of the IAM-TMD, respectively. It can be observed that for $\alpha = 0$, the transfer functions H_s and H_d recover those of the classical TMD.

First, we consider the system without damping ($\xi_s = 0$, $\xi_{id} = 0$). In this case, the transfer functions (Eqs. (9) and (10)) reduce to:

$$H_s = \frac{R_s}{P_0}, \quad H_d = \frac{R_d}{P_0}, \tag{13}$$

in which $P_0 = (2\alpha-1)(f^2-r^2)(r^2-1)-\mu f^2 r^2(2\alpha-1)^2-\alpha\beta r^2(\mu f^2(1-2\alpha)-r^2+1)$.

Figure 3a shows the amplitude of the transfer function curves of the primary structure for $f = 1$, $\mu = 0.05$, $\alpha = 0.05$ and $\theta = [15°, 20°, 30°]$. For comparison, the primary structures without TMD, with TMD and with IAM-TMD are considered. The amplitude of the transfer function of the primary structure with absorber is characterized by a frequency region where the structural response is reduced (i.e. $|H_s| < 1$) w.r.t the base motion at the structural resonance frequency

$d_g = a_g/\omega_s^2$. This frequency region, named effective zone, presents a maximum drop at the so-called anti-resonance frequency. Interestingly, it is here found that the IAM system allows for shifting the anti-resonance frequency and the related effective zone without the need to modify the mass or the static stiffness of the absorber. This is a desirable feature in the context of vibrations mitigation in civil engineering.

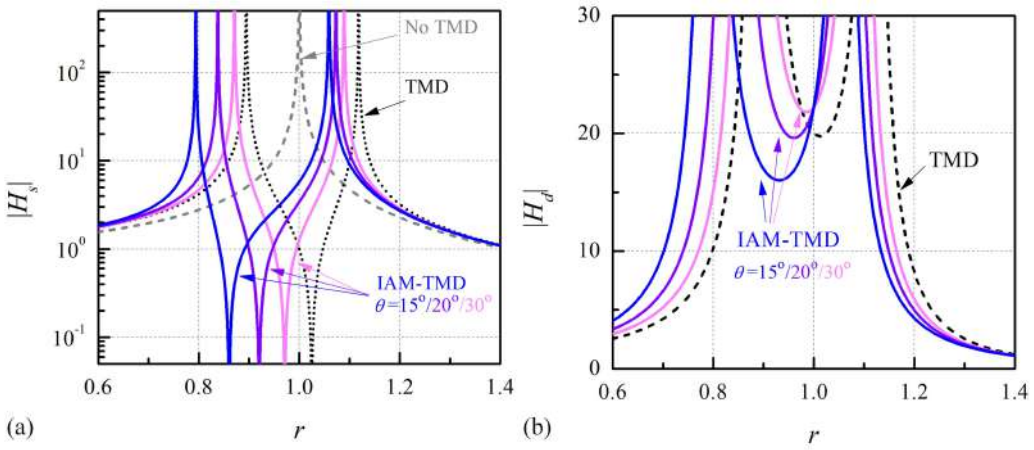

Figure 3: Amplitude of transfer functions for (a) the primary structure and (b) the absorber for the un-damped system.

Within the effective zone, the dynamic response of the main structure is attenuated because the supplied ground motion energy is absorbed mainly by the TMD. As a consequence, the relative displacement between the primary structure and the TMD is typically large, a well know critical issue in the design of the TMD. For the IAM-TMD with $\theta = 15°$, one can see in Figure 3b that the relative minimum of H_d around r=1.0 is smaller than the corresponding relative response of the TMD. In other words, with proper design, the inertial amplification mechanism system can enhance the attenuation performance of the TMD and reduce the relative displacement response of the absorber.

To investigate all the IAM-TMD configurations which outperform the response of a classical TMD, a parametric study is conducted considering the influence of the geometrical and physical parameters of the IAM on the anti-resonance frequency, effective zone and the relative minimum response of the absorber.

The anti-resonance frequency is calculated by searching for the zeros of the

transfer function H_s, yielding the closed-form expression:

$$\Omega_a = \frac{(1-2\alpha)(\mu-\alpha\mu+1)}{\sqrt{\alpha\beta-2\alpha+1}}. \tag{14}$$

The effective zone $\Delta r = r_2 - r_1$ can be obtained by equating H_s =1, which allows to define:

$$\Delta r = r_2 - r_1 = \sqrt{\frac{A_{s2}+B_{s2}}{2C_{s2}}} - \sqrt{\frac{A_{s1}-B_{s1}}{2C_{s1}}}, \tag{15}$$

in which:

$$\begin{aligned}
A_{s1} = \;& \alpha\beta(\mu f^2 - 2\alpha\mu f^2 + 2) - (2\alpha-1)(\mu f^2 - 2\mu\alpha f^2 + f^2 + 2);\\
A_{s2} = \;& -(2\alpha-1)(\mu - 2\mu\alpha f^2 + \alpha\mu\beta + 1)f^2;\\
B_{s1} = \;& \Big[\alpha\beta\Big(4\alpha(2f^2+\beta-4) + 2f^2(\mu f^2 + 2\mu - 2)\\
& -2\mu f^2(10\alpha + 4\alpha f^2 - \mu f^2 - 12\alpha^2 - 4\alpha^2 f^2\\
& -12\alpha^2\mu f^2 + 8\alpha^3\mu f^2 + 6\alpha\mu f^2)\\
& -\alpha\mu\beta f^2(2\alpha-1)(\alpha f^2 - 2\alpha\mu f^2 + 4) + 8\Big)\\
& +(2\alpha-1)^2\Big((\mu - 2\alpha\mu + 1)^2 f^4 - 4\alpha\mu f^2 - 4f^2 + 4\Big)\Big]^{1/2};\\
B_{s2} = \;& \Big[\alpha^2\mu^2\beta f^2(\beta + 24\alpha - 4\alpha\beta + 4\alpha^2\beta - 16\alpha^2)\\
& +2\mu\alpha\beta f^2(\mu - 4\alpha - 6\alpha\mu + 4\alpha^2 + 1)\\
& +4\alpha\mu\beta(2\alpha^2 - 3\alpha + 1)\\
& +8\alpha^2\mu f^2(3\mu - 2\alpha - 4\alpha\mu + 2\alpha^2\mu + 3)\\
& +(4\alpha^2 - 8\alpha\mu^2 - 12\alpha\mu - 4\alpha - 4\mu^2 + 2\mu + 1)\\
& -4\mu(2\alpha-1)^2(\alpha-1)\Big]^{1/2};\\
C_{s1} = \;& \alpha\beta - 2\alpha + 1;\\
C_{s2} = \;& C_{s1}.
\end{aligned} \tag{16}$$

In addition, the relative minimum of H_d is found by extracting the frequency for which:

$$\frac{\partial H_d}{\partial r} = 0, \tag{17}$$

and then inserting such frequency into Eq. (13), yielding to:

$$\begin{aligned}
H_d^{min} = \;& D_s\Big[(2\alpha-1)f^2 - \tfrac{\alpha+D_s-1}{\beta-1}\Big(\beta - (4\mu+2-\mu\beta-4\alpha\mu+2\alpha\beta\mu)f^2 - 2\Big)\\
& +\tfrac{(\alpha-1+D_s)^2}{\alpha^2(\beta-1)^2}\Big(-1+2\alpha-\alpha\beta\Big) + \tfrac{(\alpha-1+D_s)}{\alpha(\beta-1)}\Big(1+f^2+\mu f^2\Big)\Big]^{-1},
\end{aligned} \tag{18}$$

in which $D_s = (1-\alpha)(\alpha\beta - 2\alpha + 1) - \alpha(2\alpha - 1)(\beta - 1)(\mu - \alpha\mu + 1)f^2$.

To highlight the enhancement of the IAM performance w.r.t. the TMD, three normalized parameters, namely the normalized anti-resonance R_{Ω_a}, the normalized effective zone $R_{\Delta r}$, and the normalized absorber minimal response $R_{H_d^{min}}$, are introduced:

$$R_{\Omega_a} = \frac{\Omega_a^{\text{IAM-TMD}}}{\Omega_a^{\text{TMD}}}, \quad R_{\Delta r} = \frac{\Delta r_{\text{IAM-TMD}}}{\Delta r_{\text{TMD}}}, \quad R_{H_d^{min}} = \frac{H_d^{min}|_{\text{IAM-TMD}}}{H_d^{min}|_{\text{TMD}}}. \tag{19}$$

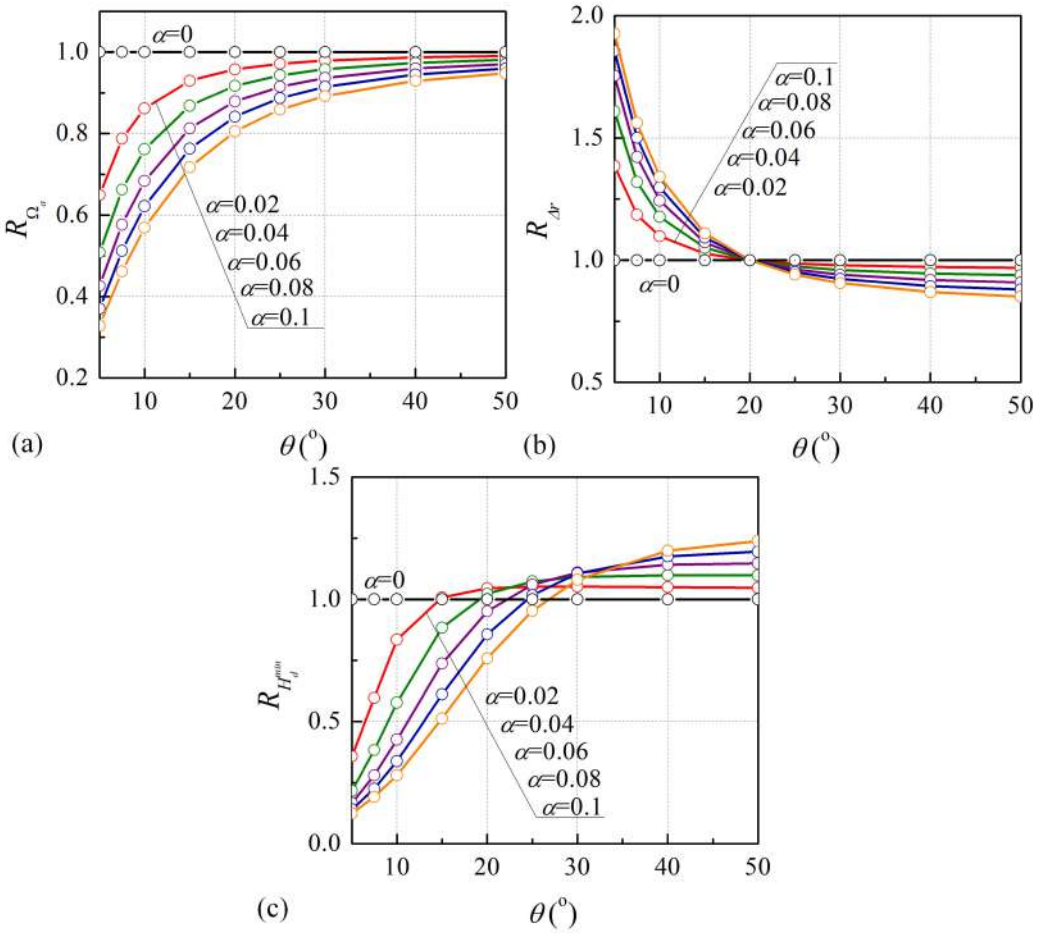

Figure 4: (a) Normalized anti-resonance frequency, (b) normalized effective zone and (c) normalized relative minimum value of H_d versus the parameters of the IAM.

Figure 4 presents the variation of the above-introduced parameters w.r.t. the IAM geometrical configuration (θ) and the mass distribution parameter (α). As

expected, these three normalized parameters equal to 1 when $\alpha = 0$, as the inertial amplification effect of the IAM disappears. From Figure 4a one can observe that the anti-resonance frequency of the primary structure is always lowered when the IAM is used (i.e., $R_{\Omega_a} < 1$), although the overall mass of the IAM-TMD equals the one of the TMD. In particular, smaller θ and lower α reduce R_{Ω_a}. Figure 4b shows the variation of the effective zone for different IAM configurations. For a given mass distribution parameter α, the IAM effective zone is larger than the corresponding TMD within the range $\theta < 20°$; this trend is further enhanced for larger values of α. Finally, Figure 4c shows the variation of the IAM-TMD relative minimum response $R_{H_d^{min}}$ w.r.t. its design parameter θ and α. It is found that for a given α, a configurational angle $\theta < 20°$ provides a reduction in the minimum relative displacement $R_{H_d^{min}} < 1.0$. Therefore, with a proper selection of the geometrical and mass distribution parameters, a significant enhancement of the IAM-TMD performance can be obtained.

3. Optimal tuning conditions for damped IAM-TMD

3.1. H_∞ optimization for harmonic excitation

H_∞ optimization aims to minimize the maximum amplitude response (the worst-case response) to sinusoidal inputs of the primary system. [3] The primary structure is modeled as an undamped SDOF equipped with a damped IAM-TMD (ξ_s=0, $\xi_{id} \neq 0$). In this case, the transfer function for the primary structure reads:

$$H_s = \frac{R_s + iI_s}{P_0 + iQ} = \frac{R_s + iI_{s0}\xi_{id}}{P_0 + iQ_0\xi_{id}}, \tag{20}$$

in which $I_{s0} = -2fr(2\alpha-1)(\mu-\mu\alpha+1)$, $Q_0 = 2fr(2\alpha-1)((\mu-2\alpha\mu+\alpha\beta\mu+1)r^2-1)$. Hence, the the amplitude of the transfer function can be expressed as:

$$|H_s| = \left|\frac{I_{s0}}{Q_0}\right| \sqrt{\frac{(R_s/I_{s0})^2 + \xi_{id}^2}{(P_0/Q_0)^2 + \xi_{id}^2}}. \tag{21}$$

According to the Fix-point theory [3], two normalized frequencies r_j ($j = 1, 2$) for which the value of H_s is equal and independent of the damping ratio ξ_{id}, exits. These two constraints require that:

$$\left(\frac{R_s}{I_{s0}}\right)^2\Big|_{r_j} = \left(\frac{P}{Q_0}\right)^2\Big|_{r_j}; \quad \left(\frac{I_{s0}}{Q_0}\right)^2\Big|_{r_1} = \left(\frac{I_{s0}}{Q_0}\right)^2\Big|_{r_2}. \tag{22}$$

In particular, the first constraint in Eq. (22) can be written as:

$$a_0 r^4 + b_0 r^2 + c_0 = 0, \tag{23}$$

in which:

$$\begin{aligned} a_0 = \;& 2f(2\alpha-1)(\alpha\beta-2\alpha+1)(2\mu-3\alpha\mu+\alpha\beta\mu+2); \\ b_0 = \;& 4f^3(2\alpha-1)^2(\mu-\alpha\mu+1)(\mu-2\alpha\mu+\alpha\beta\mu+1) \\ & -2f(2\alpha-1)(\alpha\beta-2\alpha+1)(\mu-\alpha\mu+2); \\ c_0 = \;& -4f^3(2\alpha-1)^2(\mu-\alpha\mu+1). \end{aligned} \tag{24}$$

Based on Eq. (23), the sum of the squared values of the two frequencies $r_{1,2}$ can be obtained as:

$$r_1^2 + r_2^2 = -\frac{b_0}{a_0}. \tag{25}$$

For the second constrain in Eq. (22), the sum of the squared values of the two frequencies $r_{1,2}$ yields:

$$r_1^2 + r_2^2 = -\frac{2b_0^{'}}{a_0^{'}}, \tag{26}$$

where

$$\begin{aligned} a_0^{'} = \;& (\mu-2\alpha\mu+\alpha\beta\mu+1)/(\mu-\alpha\mu+1); \\ b_0^{'} = \;& -1/(\mu-\alpha\mu+1). \end{aligned} \tag{27}$$

By coupling Eqs. (25) and (26), the optimal tuning ratio f_{opt} is obtained:

$$f_{opt} = \sqrt{\frac{(\alpha\beta-2\alpha+1)[\mu(\alpha-1)(\mu(\alpha\beta-2\alpha+1)-1)+2]}{2(1-2\alpha)(\mu-\alpha\mu+1)[\mu(\alpha\beta-2\alpha+1)+1]^2}}, \tag{28}$$

and by inserting f_{opt} into Eq. (23) yields the closed-form expressions of the frequency locations of the two fixed points:

$$r_{1,2} = \sqrt{\frac{S \pm \sqrt{\mu(\mu-\alpha\mu+1)(\alpha\beta-2\alpha+1)S}}{\alpha^2\mu^2(\beta^2-5\beta+6)+(3\alpha\mu\beta-7\alpha\mu)(\mu+1)+2(\mu+1)^2}}, \tag{29}$$

in which $S = 2\mu - 3\alpha\mu + \alpha\mu\beta + 2$.

At this stage, substituting the optimal tuning ratio f_{opt} into the second constraint of Eq. (22), the transfer function at the two fixed points are obtained as:

$$H_s\Big|_{r_{1,2}} = \sqrt{\frac{(\mu-\alpha\mu+1)(2\mu-3\alpha\mu+\alpha\mu\beta+2)}{\mu(\alpha\beta-2\alpha+1)}}. \tag{30}$$

By varying the damping coefficient of the absorber, one may find that the transfer function passes through the two fixed points with a different gradient. The optimal damping ratio ξ_{id}^{opt} corresponds to the special case where the transfer function has a maximum at one of the fixed points, i.e., a null derivative at r_1 or r_2:

$$\left.\frac{\partial H_s}{\partial r}\right|_{r_1} = 0, \quad \left.\frac{\partial H_s}{\partial r}\right|_{r_2} = 0. \tag{31}$$

By solving Eq. (31), the two damping ratios ξ_{d1} and ξ_{d2} are found. Indeed, for the design of the dashpot, only one damping ratio is needed. Typically, the root mean square (rms) of the two values is chosen [3]:

$$\xi_{id}^{opt} = \sqrt{\frac{\xi_{id1}^2 + \xi_{id2}^2}{2}} = \sqrt{\frac{\psi(\mu(2\alpha - \alpha\beta + 1))}{8\chi(2\alpha - 1)(\mu - \alpha\mu + 1)}}, \tag{32}$$

in which:

$$\begin{aligned} \psi = \; & -\alpha^3\mu^2\beta^2 + \alpha^2\mu^2\beta^2 + 9\alpha^3\mu^2\beta - 16\alpha^2\mu^2\beta - 13\alpha^2\mu\beta + 7\alpha\mu^2\beta \\ & +13\alpha\mu\beta + 6\alpha\beta - 14\alpha^3\mu^2 + 33\alpha^2\mu^2 + 25\alpha^2\mu - 25\alpha\mu^2 - 37\alpha\mu \\ & -12\alpha + 6\mu 2 + 12\mu + 6; \\ \chi = \; & \alpha^3\mu^3\beta^2 - \alpha^2\mu^3\beta^2 - 4\alpha^3\mu^3 + 6\alpha^2\mu^3\beta - 2\alpha\mu^3\beta + 2\alpha\mu\beta \\ & +4\alpha^3\mu^3 - 8\alpha^2\mu^3 + 5\alpha\mu^3 - 5\alpha\mu^3 - \mu^3 + 3\mu + 2. \end{aligned} \tag{33}$$

We now consider the transfer function of the absorber. By inserting $\xi_s = 0$ into the transfer function Eq. (10), we have:

$$H_d = \frac{R_d}{P_0 + iQ_0\xi_{id}}. \tag{34}$$

In general, H_d is a function of ξ_{id}. However, for $Q_0 = 0$, H_d is independent from the damping ratio ξ_{id}, resulting in a fixed point (r_3) for the transfer function of the absorber. Solving the equation $Q_0 = 0$, the frequency location r_3 and the value of $H_d|_{r_3}$ are found:

$$r_3 = \frac{1}{\sqrt{\mu - 2\alpha\mu + \alpha\mu\beta + 1}}, \quad H_d|_{r_3} = \frac{R_d}{P_0}. \tag{35}$$

Figure 5a displays the amplitude of the transfer function of the primary structure for the system with an IAM-TMD with optimal tuning frequency and different values of damping ratio, assuming $\alpha = 0.05$, $\mu = 0.05$ and $\theta = 10°$. As expected,

when the optimized tuning ratio is considered, the amplitude of the transfer function of the primary structure passes always through the two fixed points with the same height. When ξ_{id}=0, the amplitude of the transfer function is unbounded at its eigen frequencies. By increasing of the damping ratio ξ_{id}, the responses around the system resonances are suppressed, while the responses around the anti-resonant frequency are increased. For the optimal damping ratio $\xi_{id}^{opt} = 0.24$ the minimum value of the maximum amplitude response of the primary structure is found $H_s|_{r_{1,2}} = 5.08$. In the limit case of an infinite damping ratio, the primary structure and the absorber are tied together, and the two DOF system reduces to a SDOF system. Figure 5b shows the amplitude of the transfer functions of the absorber. Similarly to the structural response, for small damping ratios, it is found that the response of the absorber around the two system eigen frequencies is very large. By increasing the damping ratio, responses around the two eigen frequencies are decreased. When the damping ratio is very large, the response of the absorber peaks at the fixed point r_3 (with the limit case for $\xi_{id} = +\infty$ for which the response of the absorber is always null except for the fixed point (r_3)).

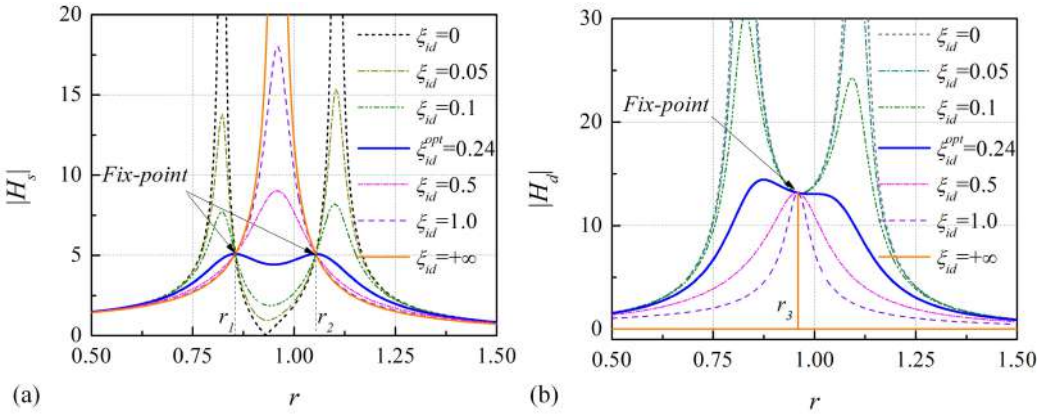

Figure 5: Amplitude of the transfer functions for (a) the primary structure and (b) the absorber for a SDOF system with the IAM-TMD.

Figure 6a compares the amplitude of the optimized transfer functions for a structure equipped with a TMD with $\mu = 0.05$ and the corresponding IAM-TMDs of $\alpha = 0.05$, $\theta = [5°, 10°]$. The optimal tuning ratios for the system with TMD and IAM-TMDs are 0.94, 1.76 ($\theta = 5°$), 1.26 ($\theta = 10°$), respectively. Here, we note that, due to the mass amplification effect of the IAM system, the optimal tuning ratios for the IAM-TMDs are larger than that of the TMD. Similarly, it is found that the optimal damping ratio of the TMD ($\xi_d = 0.14$) is smaller than those of

the IAM-TMDs ($\xi_{id} = 0.24$ for $\theta = 10°$ and $\xi_{id} = 0.56$ for $\theta = 5°$). This suggests that the proposed IAM system can enhance the energy dissipation property of the absorber.

Next, the amplitude of the transfer function of the relative displacement response between the primary structure and the absorber is considered (Figure 6b). As mentioned above, the relative displacement response between the primary structure and the absorber is a governing parameter in the design of TMDs, and small relative displacements of the absorber are always desired in the actual design. It is found that, when the classical TMD is used, the maximum relative displacement response of the absorber is 24.73. However, when the IAM-TMDs with $\theta = 10°$ and $\theta = 5°$ are considered, the maximum relative displacement responses of the absorber are 14.44 (i.e. a reduction of almost 50%) and 6.52 (i.e. a reduction of almost 70%), respectively.

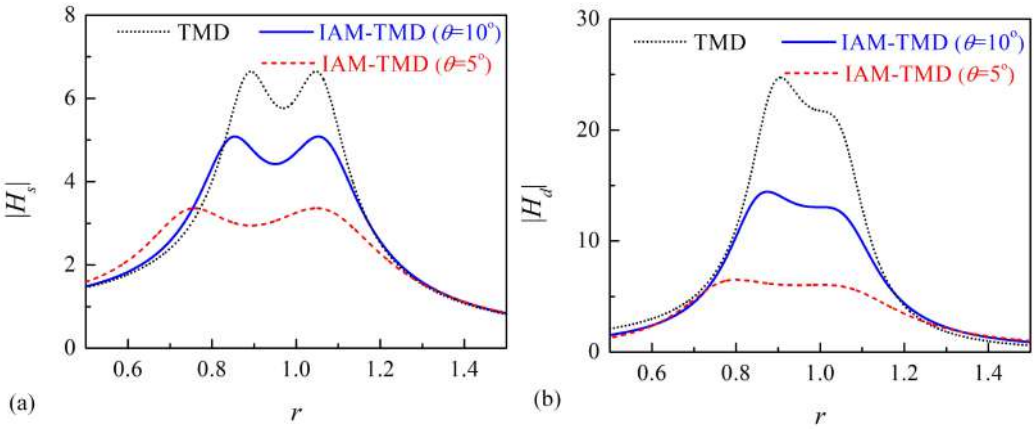

Figure 6: Optimized transfer function amplitude for (a) the primary structure and (b) the absorber for the system with TMD or IAM-TMDs.

Furthermore, the effects of the geometrical parameter θ and the mass distribution parameter α on the maximum displacement response of the main structure ($max(H_s^{opt})$) and the maximum relative displacement response of the absorber ($max(H_d^{opt})$) are presented in Figure 7. The case $\alpha = 0$, i.e. TMD, is here reported as a reference:

$$R_{H_s^{opt}} = \frac{max(H_s^{opt})|_{\text{IAM-TMD}}}{max(H_s^{opt})|_{\text{TMD}}}, \quad R_{H_d^{opt}} = \frac{max(H_d^{opt})|_{\text{IAM-TMD}}}{max(H_d^{opt})|_{\text{TMD}}}. \tag{36}$$

First, one can notice that there exists a critical θ_c around 30° at which $R_{H_s^{opt}} = 1$ and $R_{H_d^{opt}} = 1$ for any mass distribution parameter. For angles below the θ_c, $R_{H_s^{opt}}$

and $R_{H_d^{opt}}$ are smaller than 1 and decrease with a reduction of θ. For example, for $\alpha = 0.05$ and $\theta = 10°$, $R_{H_s^{opt}}$ displays a reduction of about 20% and $R_{H_d^{opt}}$ shows a reductions of more than 40%. Comparing Figure 7a and Figure 7b, we can observe that the effect of the IAM is always more significant on the absorber response $R_{H_d^{opt}}$ than on the structural one $R_{H_s^{opt}}$. Conversely for angles larger than θ_c, both $R_{H_s^{opt}}$ and $R_{H_d^{opt}}$ increase gradually with the increase of θ, leading to a reduced effect of the proposed IAM system w.r.t. the classical TMD. As expected, the effect of the IAM system is amplified when larger mass ratio are considered.

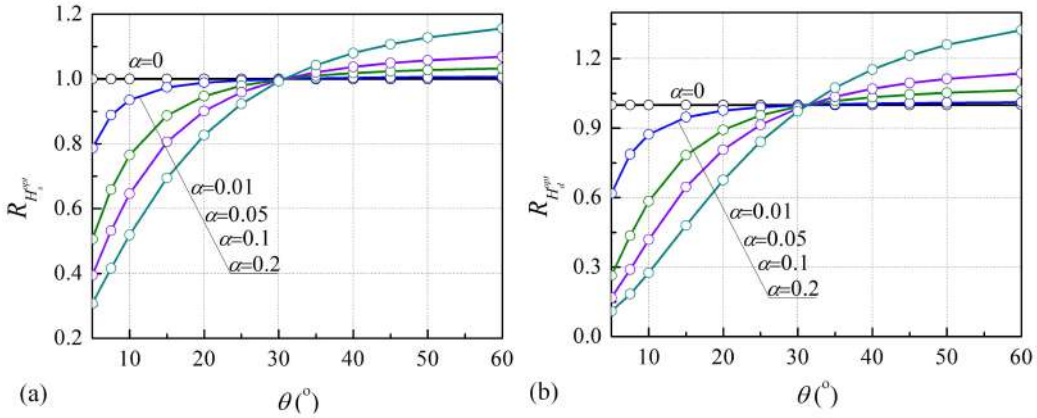

Figure 7: (a) $R_{H_s^{opt}}$ and (b) $R_{H_d^{opt}}$ versus the geometrical parameter θ and the mass distribution parameter α of the IAM.

3.2. H_2 optimization for random excitation

H_2 optimization aims at minimizing the total vibration energy of the system over all frequencies. Hence, when the system is subjected to random instead of sinusoidal ground motion excitation, the H_2 optimization is more effective than the H_∞ optimization [6, 7, 11, 15]. In this section, the optimal IAM-TMD design parameters are derived in closed-form for an undamped SDOF primary structure under white noise base excitation.

Consider the dynamic responses of the primary structure with TMD or IAM-TMD under the normalized stationary stochastic excitation process $a_g(t)/\omega_s^2$. In the frequency domain, the stochastic excitation can be represented via a double-sided spectral density function, i.e., power spectrum, $S(\omega)$. The ideal white noise process with a constant power spectrum over all frequencies $S(\omega) = S_0$ is here considered. Hence, the variance of the displacement responses of the primary

structure can be computed as:

$$\sigma_s^2 = \int_{-\infty}^{+\infty} |H_s(\omega)|^2 S(\omega) d\omega = S_0 \omega_s \int_{-\infty}^{+\infty} |H_s(ir)|^2 dr. \tag{37}$$

The performance of the primary structure can be evaluated by using the H_2 norm of the stable transfer function $\hat{H}_s(s)$:

$$\Phi = \frac{\sigma_s^2}{2\pi S_0 \omega_s} = \frac{1}{2\pi} \int_{-\infty}^{+\infty} |H_s(ir)|^2 dr = |\hat{H}_s(s)|_2^2, \tag{38}$$

where, $\hat{H}_s(s)$ is the Laplace form of the transfer function $H_s(ir)$. The H_2 norm of the stable transfer function $\hat{H}_s(s)$ is here calculated by using the analytic approach developed in the linear control theory [12]. Details are given in Appendix-A. We derive the optimal TMD tuning ratio f and damping ratio ξ_{id}, by minimizing Φ:

$$\frac{\partial \Phi}{\partial \xi_{id}} = 0, \quad \frac{\partial \Phi}{\partial f} = 0. \tag{39}$$

For the considered system, Φ can be written as:

$$\Phi = F(f)\xi_{id} + \frac{G(f)}{\xi_{id}}, \tag{40}$$

in which $F(f)$ and $G(f)$ are functions of f given in Appendix-A.

By inserting Eq. (40) into the first partial equation of Eq. (39), the optimal damping ratio ξ_{id}^{opt} and the minimum performance measure Φ_{opt} can be given as functions of the optimal tuning ratio f_{opt}:

$$\xi_{id}^{opt} = \sqrt{\frac{G(f_{opt})}{F(f_{opt})}}, \quad \Phi_{opt} = 2\sqrt{F(f_{opt})G(f_{opt})}. \tag{41}$$

Then, inserting Eq. (41) into the second partial equation of Eq. (39), the optimal tuning ratio f_{opt} can be obtained:

$$f_{opt} = \sqrt{\frac{(\alpha\beta - 2\alpha + 1)[\mu(\alpha\beta - 2\alpha + 1)(\mu - \alpha\mu + 1) + 2]}{2(1 - 2\alpha)(\mu - \alpha\mu + 1)[\mu(\alpha\beta - 2\alpha + 1) + 1]^2}}. \tag{42}$$

Substituting the optimal tuning ratio f_{opt} into Eq. (41), the optimal damping ratio ξ_{id}^{opt} and the minimum performance measure Φ_{opt} are obtained:

$$\xi_{id}^{opt} = \sqrt{\frac{\mu[\mu(\alpha\beta - 2\alpha + 1)(\alpha\mu - \mu + 3) + 4](\alpha\beta - 2\alpha + 1)^2}{8(1 - 2\alpha)[\mu(\alpha\beta - 2\alpha + 1)\kappa + 2]}}, \tag{43}$$

$$\Phi_{opt} = \sqrt{\frac{[4+\mu(\alpha\beta-2\alpha+1)(\alpha\mu-\mu+3)](1-\alpha\mu+\mu)^3}{4\mu(\alpha\beta-2\alpha+1)(\mu-2\alpha\mu+\alpha\beta\mu+1)}}, \tag{44}$$

with $\kappa = \mu^2(\alpha-1)(\alpha\beta-2\alpha+1)+\alpha\beta\mu-\alpha\mu+3$.

Equipped with the optimal parameters according to the H_2 optimization, we evaluate the effects of the IAM design parameters by introducing the three normalized parameters:

$$R_\Phi = \frac{\Phi^{opt}_{\text{IAM-TMD}}}{\Phi^{opt}_{\text{TMD}}}, \quad R_\xi = \frac{\xi^{opt}_{\text{IAM-TMD}}}{\xi^{opt}_{\text{TMD}}}, \quad R_f = \frac{f^{opt}_{\text{IAM-TMD}}}{f^{opt}_{\text{TMD}}}. \tag{45}$$

Figure 8 shows the variation of the three normalized parameters versus the geometrical parameter θ and the mass distribution parameter α. Again the case $\alpha = 0$, for which these three parameters equal to 1, is considered as a reference. As for the H_∞ optimization, the critical angle $\theta_c \approx 30°$ discriminates between the IAM-TMD configurations with enhanced performance reduction (i.e. $R_\Phi < 1$ for $\theta < \theta_c$) w.r.t. the TMD. In addition, Figure 8b and 8c show that the normalized optimal tuning ratio and damping ratio of the IAM-TMD system are always larger than 1. In other words, the optimal damping and stiffness of the absorber are enlarged by the IAM system. However, similarly to what observed for the H_∞ optimization, the H_2 performance can only be enhanced within a specific range of θ. Therefore, in actual design the geometrical parameter of the IAM system should be considered carefully.

Finally, the optimal parameters f_{opt} and ξ_{opt} as obtained from the H_∞ and H_2 optimization processes are compared in Figure 9. As previously discussed, since the IAM system can enhance the performance of the TMD within the angle range $\theta < \theta_c$, only these configurations are considered for a meaningful comparison. It is here remarked that when $\alpha = 0$, i.e. the TMD system, the optimal tuning ratios in the H_2 and H_∞ optimizations are the same (Figure 9a), while the optimal damping ratio in the H_2 optimization is smaller than the related one in the H_∞ optimization (Figure 9b). When $\theta > 0°$ the amplification effect of the IAM system is included, and the optimal parameters in the two optimizations are different. For the optimal tuning ratio f_{opt}, it is found in Figure 9a that the optimal value in the H_2 optimization is larger than that in the H_∞ optimization, especially for cases with small θ and large α. For the damping ratio, the optimal value in the H_2 optimization is smaller than that in the H_∞ optimization, particularly when $\theta < 20°$. We underline that the two optimal parameters for IAM-TMD are always significantly larger than the related TMD ones.

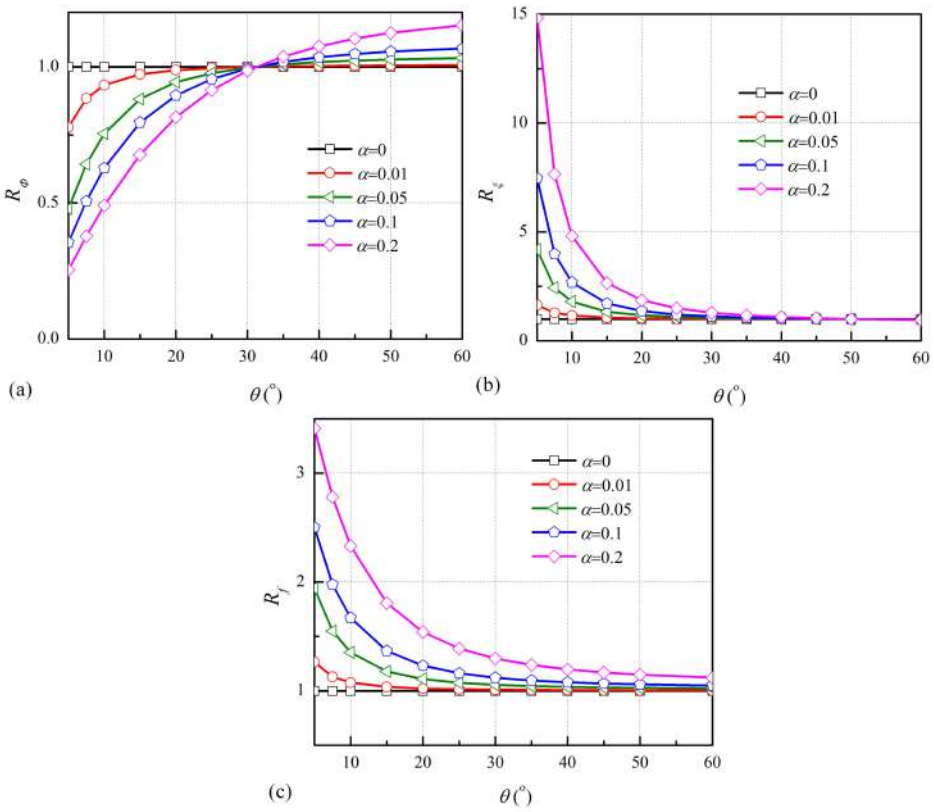

Figure 8: (a) R_Φ, (b) R_ξ and (c) R_f versus the geometrical parameter θ and the mass distribution parameter α of the IAM.

4. Time history analysis

In this section, time history analyses are conducted to validate the efficiency of the proposed IAM-TMD system. The governing equations of the systems are setup in a MATLAB environment and solved by using the Newmark-β method. Three primary structures (without TMD, with TMD and with IAM-TMD) are considered. For all the performed time histories, it is assumed that the structures are at rest for $t = 0$ s. For the primary structure, the following normalized parameters are assumed: $\omega_s = 2\pi$, $\xi_s = 0$. For both the TMD and the IAM-TMD, the mass ratio is $\mu = 0.05$. Besides, the geometrical parameter and the mass distribution parameter of the IAM-TMD are $\theta = 10°$ and $\alpha = 0.1$, respectively. Performing the H_∞ and H_2 optimization, the optimal parameters of the TMD and the IAM-TMD are obtained and given in Table 1.

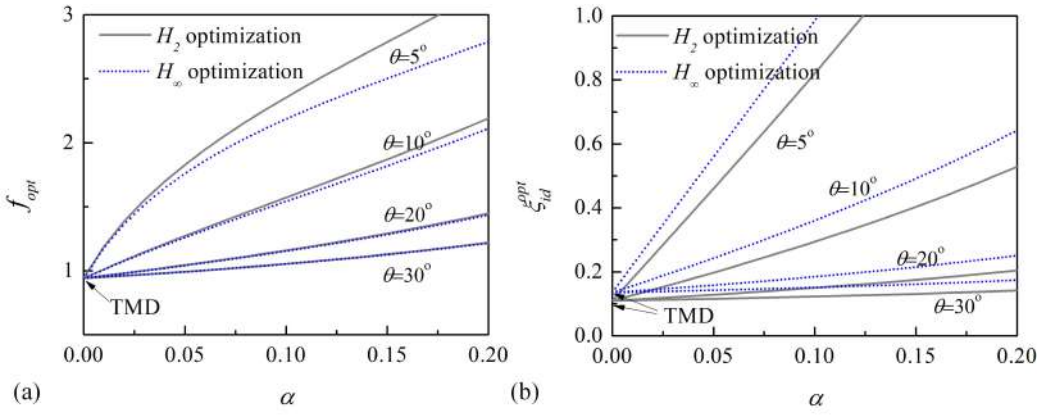

Figure 9: Optimal (a) tuning ratio, (b) damping ratio in the H_2 and H_∞ optimizations.

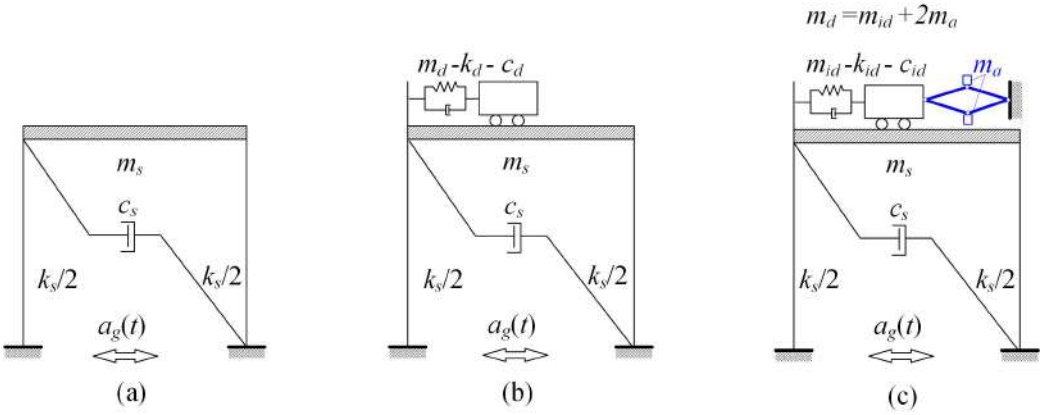

Figure 10: A shear type frame structure under ground motion (a) without TMD, (b) with TMD and (c) with IAM-TMD.

Table 1: Optimal parameters of the TMDs

Name	Optimization methods	f_{opt}	ξ_{opt}	Fixed points($r_{1/2}$)
TMD	H_∞	0.94	0.135	0.895/1.05
TMD	H_2	0.94	0.11	-
IAM-TMD	H_∞	1.54	0.36	0.855/1.05
IAM-TMD	H_2	1.57	0.29	-

4.1. Harmonic ground motion excitation

First, the harmonic acceleration ground motion ($a_g(t) = a_g cos(\omega t)$) with its frequency at the fixed point, i.e., $r_2 = 1.05$, is imposed. Figure 11a shows the

normalized displacement responses of the primary structure (H_s). As expected, the primary structure without any vibration absorber shows a typical beating phenomenon and consequently a large response. When the TMD and IAM-TMD are used, the responses of the primary structure are mitigated, with a larger reduction provided by the IAM-TMD, as predicted by the H_∞ optimization. The beneficial effect of the IAM is also evident in the reduction of the normalized relative displacement responses of the absorber, as shown in Figure 11b.

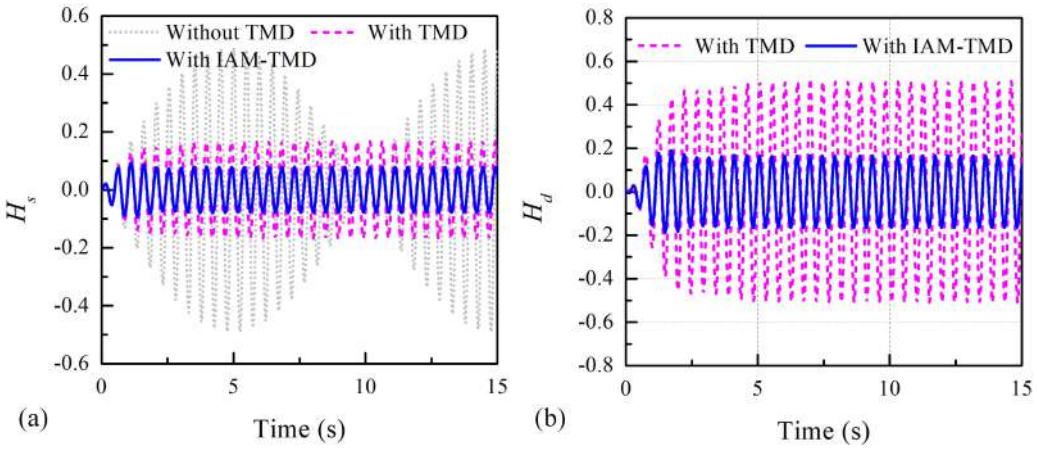

Figure 11: Normalized (a) displacement responses of the primary structure and (b) the relative displacement of the absorber with respect to the primary structure with the considered three systems under a harmonic ground motion input at the fixed point $r_2 = 1.05$.

In addition, the influence of the optimization method on the dynamic responses of the primary structure with IAM-TMD is investigated, and the results are presented in Figure 12. Here, the harmonic acceleration ground motion with its frequency at the fixed point $r_1 = 0.855$ is considered. As expected, by using the H_∞ optimization, the peak values of the H_s and H_d are slightly reduced w.r.t. those of the IAM-TMD designed using the H_2 optimization. In particular, the relative displacement response between the primary structure and the absorber is more sensitive to the optimization method than the displacement response of the primary structure.

4.2. Seismic ground motion excitation

In Section 3.2, the optimal design of the IAM-TMD has been sought by considering the ground motion excitation as a stationary white-noise process. Earthquake ground motion is indeed an example of random ground motion excita-

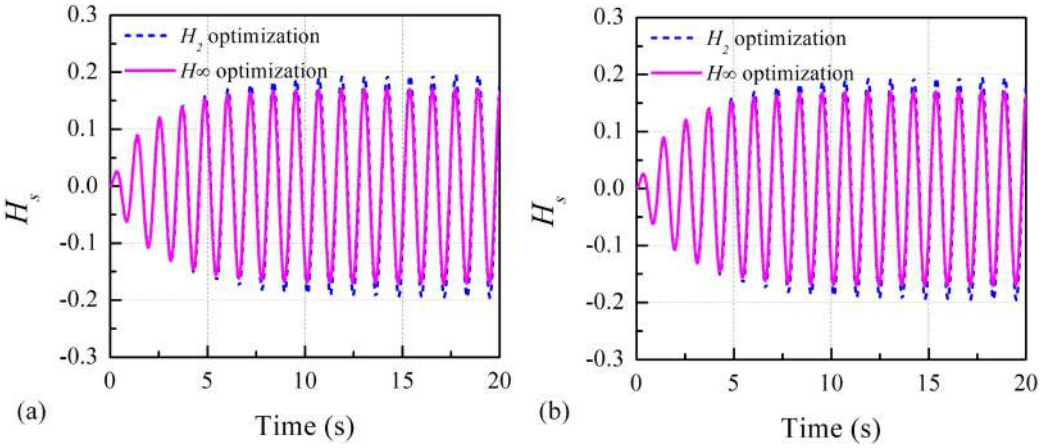

Figure 12: Normalized (a) displacement responses of the primary structure and (b) relative displacement of the absorber with respect to the primary structure with the considered systems under a harmonic ground motion input ($r_1 = 0.855$) using the H_∞ and H_2 optimization methods.

tion in engineering. However, it must be pointed out that real earthquake motions are neither stationary nor have a uniform spectral content, as the simple case of white-noise inputs. Therefore, time history analyses performed with real recorded accelerograms are always needed to account for the non-stationary nature of the seismic input [44] and to test the performance of the absorbers under such inputs. As shown in Table 2 and Table 3, ten far-field and ten near-field natural earthquake records, respectively, are considered in this study. These accelerograms were downloaded from the Pacific Earthquake Engineering Research Center/PEER Ground Motion Database (https://ngawest2.berkeley.edu). Two selected far-field records (ELC180 and RCH190) and two selected near-field records (CLS090 and TCU065E) are depicted in Figure 13a, meanwhile, their spectral characteristics are shown in Figure 13b.

As the H_2 optimization aims at minimizing the vibration energy of the system over all frequencies, the root mean square of the displacement responses of the primary structure H_s^{rms} and the root mean square of the relative displacement response of the absorber H_d^{rms} are here considered to evaluate the effectiveness of the proposed IAM-TMD system. In addition, the maximum absolute displacement response of the primary structure $|H_s|^{max}$ and the maximum absolute relative displacement response of the absorber $|H_d|^{max}$ are also considered.

The normalized displacement responses of the primary structure H_s for these four accelerograms are given in Figure 14a. As can be seen, the IAM-TMD over-

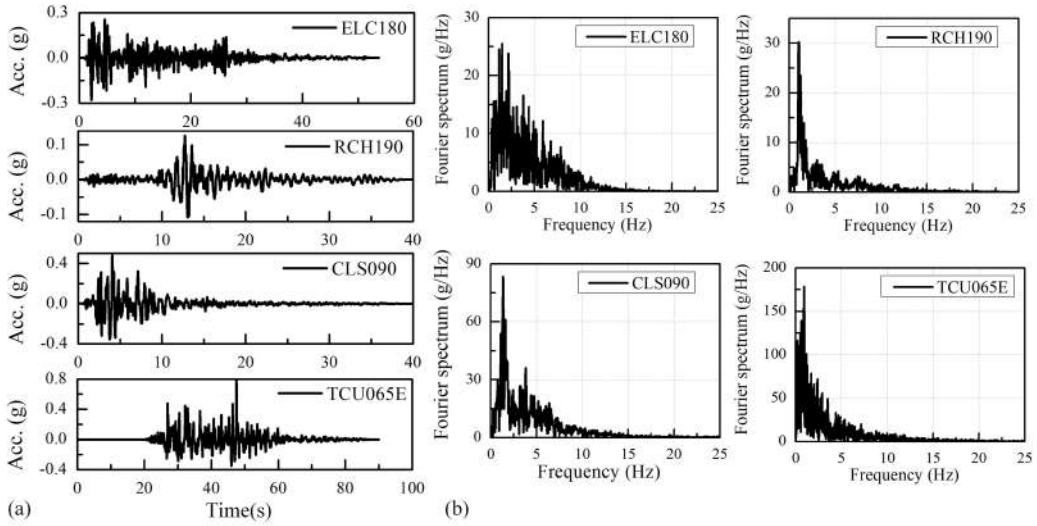

Figure 13: (a) Acceleration time histories of the ELC-180 and the RCH190 (two examples of the 10 selected far-filed records), the CLS090 and TCU065E (two examples of the 10 selected near-filed records) and (b) their Fourier spectrum.

Table 2: Ten far-filed earthquake records(source: https://ngawest2.berkeley.edu)

Earthquake	Date	M_w	Record Station	Component	PGA,g
Imperial Valley	1940-05-19	6.95	El Centro	ELC180	0.28
Imperial Valley	1940-05-19	6.95	El-Centro	ELC270	0.21
San Fernando	1971-02-09	6.61	Maricopa	MA1220	0.01
San Fernando	1971-02-09	6.61	Maricopa	MA1130	0.007
Northridge	1994-01-17	6.69	UCLA	UCL090	0.28
Northridge	1994-01-17	6.69	UCLA	UCL360	0.47
Kobe	1995-01-16	6.9	Amagasaki	AMA090	0.33
Kobe	1995-01-16	6.9	Amagasaki	AMA000	0.28
Loma Prieta	1989-10-18	6.93	R.City Hall	RCH190	0.13
Loma Prieta	1989-10-18	6.93	R.City Hall	RCH280	0.11

performs the other two cases. To better highlight the dynamic response of the TMD and IAM-TMD, the Fourier spectra of the considered cases are shown in Figure 14b. As expected, the use of the TMD suppresses the responses of the primary structure around its eigen frequency. By introducing the IAM system, the dynamic responses of the primary structure are further reduced.

Figures 15a and 16a show the H_s^{rms} with the three structures, normalized by the

Table 3: Ten near-filed earthquake records(source: https://ngawest2.berkeley.edu)

Earthquake	Date	M_w	Record Station	Component	PGA,g
Loma Prieta	1989-10-18	6.93	Corralitos	CLS090	0.48
Loma Prieta	1989-10-18	6.93	Corralitos	CLS000	0.64
Imperial Valley	1979-10-15	6.53	B. Airport	BRA315	0.22
Imperial Valley	1979-10-15	6.53	B. Airport	BRA225	0.16
Northridge	1994-01-17	6.69	LA-Dam	LDM334	0.32
Northridge	1994-01-17	6.69	LA-Dam	LDM064	0.43
Morgan Hill	1984-04-24	6.19	Corralitos	CLS220	0.08
Morgan Hill	1984-04-24	6.19	Corralitos	CLS310	0.11
Chi-Chi	1999-09-24	7.62	TCU065	TCU065N	0.58
Chi-Chi	1999-09-24	7.62	TCU065	TCU065E	0.79

H_s^{rms} of the structure without TMD, under the considered far-field and near-field earthquake inputs, respectively. It can be seen that performances of the primary structure with TMDs vary from case to case since they are strictly dependent on the frequency content of the considered input. Overall, the responses for TMD or IAM-TMD are smaller than 1 for the considered inputs. On average, a reduction of 60% and 75% are attained for the primary structure with TMD and IAM-TMD, respectively.

Figures 15b and 16b show the normalized $|H_s|^{max}$ for the three structures under the considered far-field and near-field earthquake inputs, respectively. It can be observed that apart for the case AMA090 the maximum structural response is reduced by using TMD or IAM-TMD. On average, a reduced response of 62% and 53% is observed for the system with TMD and IAM-TMD, respectively. When the AMA090 record is input into the system, the maximum displacement responses of the primary structure with TMD or IAM-TMDs are 106% and 101%, respectively. That is to say, the TMD system amplifies the maximum absolute displacement response of the primary structure. Indeed, this is an expected consequence of the H_2 optimization which aims at mitigating the total energy input into the system, not the maximum of the displacement response. Nonetheless, even in this case, the displacement of the primary structure with IAM-TMD is slightly smaller than those with the TMD.

Finally, the relative displacement responses of the absorber with respect to the primary structure H_d are investigated. Similar to Figure 14, Figure 17a shows the time histories of the normalized relative displacement responses of the absorber, and Figure 17b presents the corresponding Fourier spectra. The relative displace-

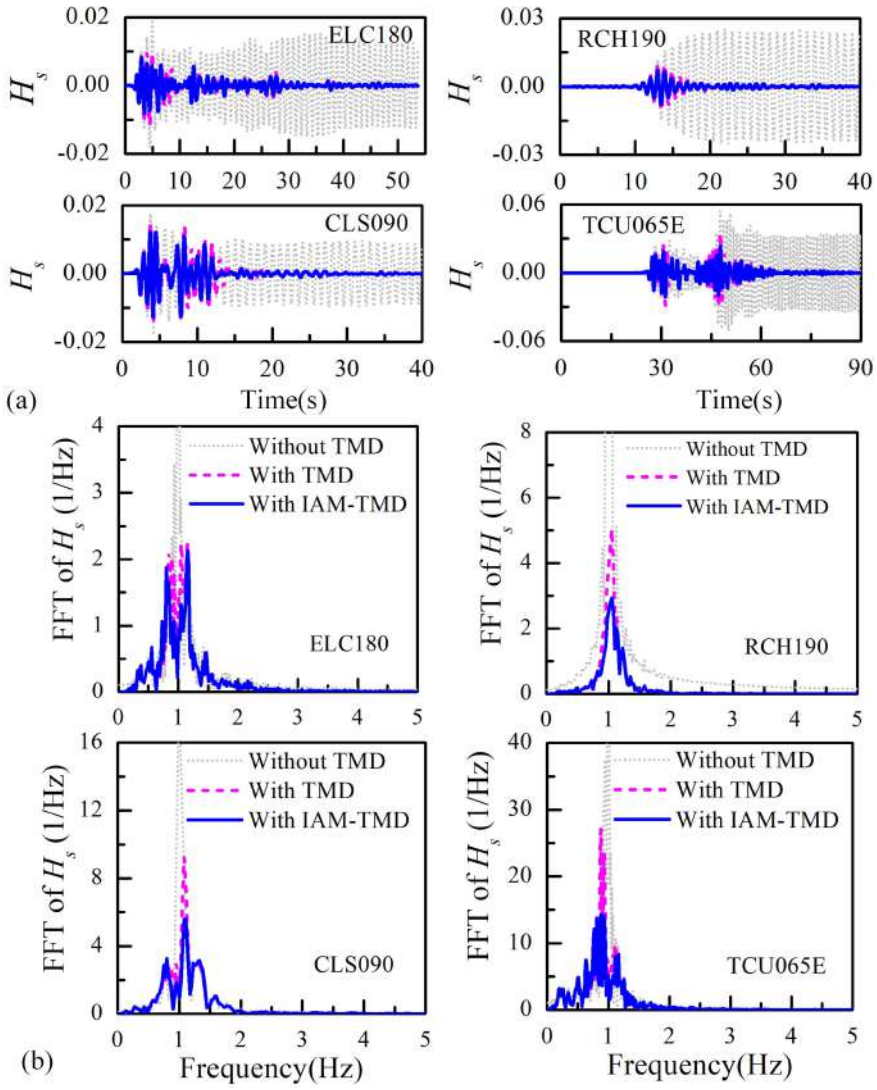

Figure 14: Normalized (a) displacement responses of the primary structures and (b) their Fourier spectrum with the considered three systems under different earthquake inputs.

ment responses of the absorber are significantly reduced by the addition of the IAM system. In the frequency domain, responses of the absorber are mainly restricted in a small region around the eigen frequency of the primary structure, in which the IAM-TMD over-perform w.r.t. the TMD. Out of this region, the responses of the absorber are very small and can be ignored.

Figures 18a and 19a show the normalized H_d^{rms} for the three systems under

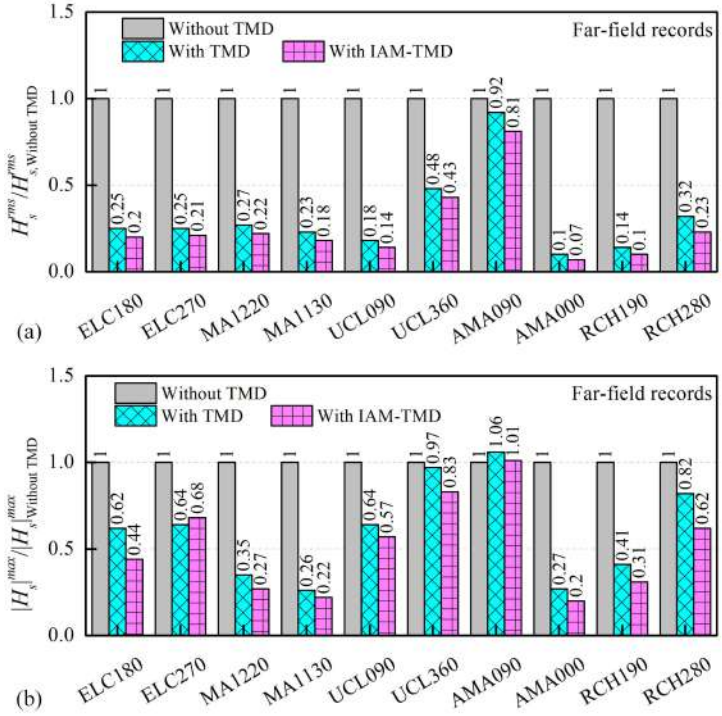

Figure 15: Normalized (a) root mean square and (b) maximum absolute displacement responses of the primary structure under the considered far-field earthquake inputs.

the considered far-field and near-field earthquake inputs, respectively. Here the responses are normalized by the related value with TMD. On average, a reduction of 47% is achieved, which means the energy input into the IAM-TMD is almost half of that of TMD. The normalized $|H_d|^{max}$ are given in Figures 18b and 19b. Also for this parameter an average reduction of 40% is obtained.

5. Conclusions

In this paper, a novel TMD equipped with an inertial amplification mechanism is proposed to achieve enhanced vibration mitigation performance.

The proposed inerter-like system has a mass amplification effect related to its geometrical configuration and mass distribution. Comparing to the TMD system, the proposed IAM-TMD system can amplify the apparent mass of the absorber without increasing the actual mass of the system. In particular, when a configurational angle θ below 20° is chosen, the IAM-TMD anti-resonance frequency shifts

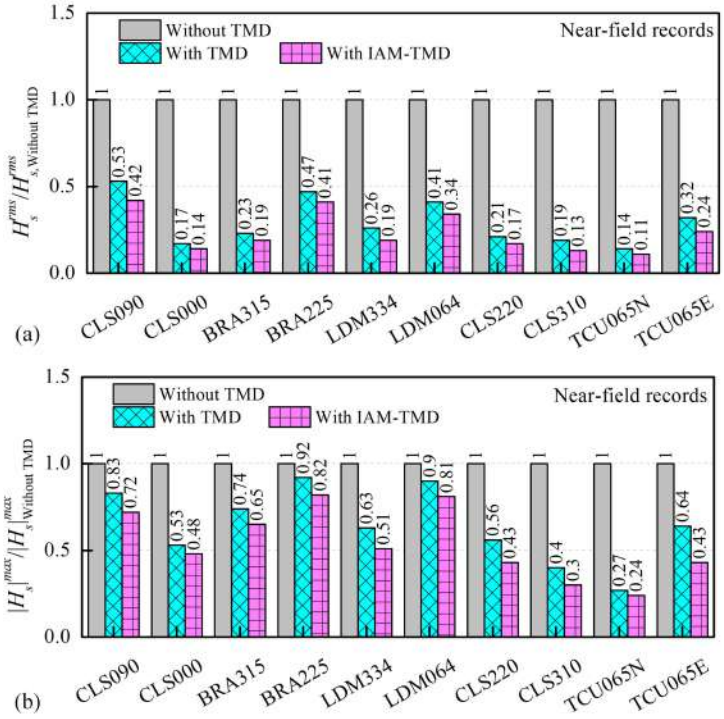

Figure 16: Normalized (a) root mean square and (b) maximum absolute displacement responses of the primary structure under the considered near-field earthquake inputs.

towards lower frequency values and the width of the effective zone is enlarged. Additionally, the relative responses of the absorber can be notably reduced.

For a harmonic ground motion, the H_∞ optimization (i.e., the Fixed-point theory) is utilized to optimize the performance of the IAM-TMD system. Closed-form solutions for the optimal design parameters of the IAM-TMD have been obtained, together with frequency locations of the fixed-points as well as peak values of the transfer functions. Thanks to the inertial amplification effect of the IAM, it is observed that the optimal turning ratio and damping ratio of the IAM system are much larger than those of the TMD. When $\theta < \theta_c \approx 30^\circ$, both the peak value of the displacement transfer function of the primary structure and the peak value of the transfer function of the relative displacement responses of the absorber are suppressed.

For a random white-noise ground motion, the H_2 optimization is employed to evaluate the performance of the IAM-TMD. Closed-form solutions for the optimal design parameters and the performance measures are obtained. Similar to the H_∞

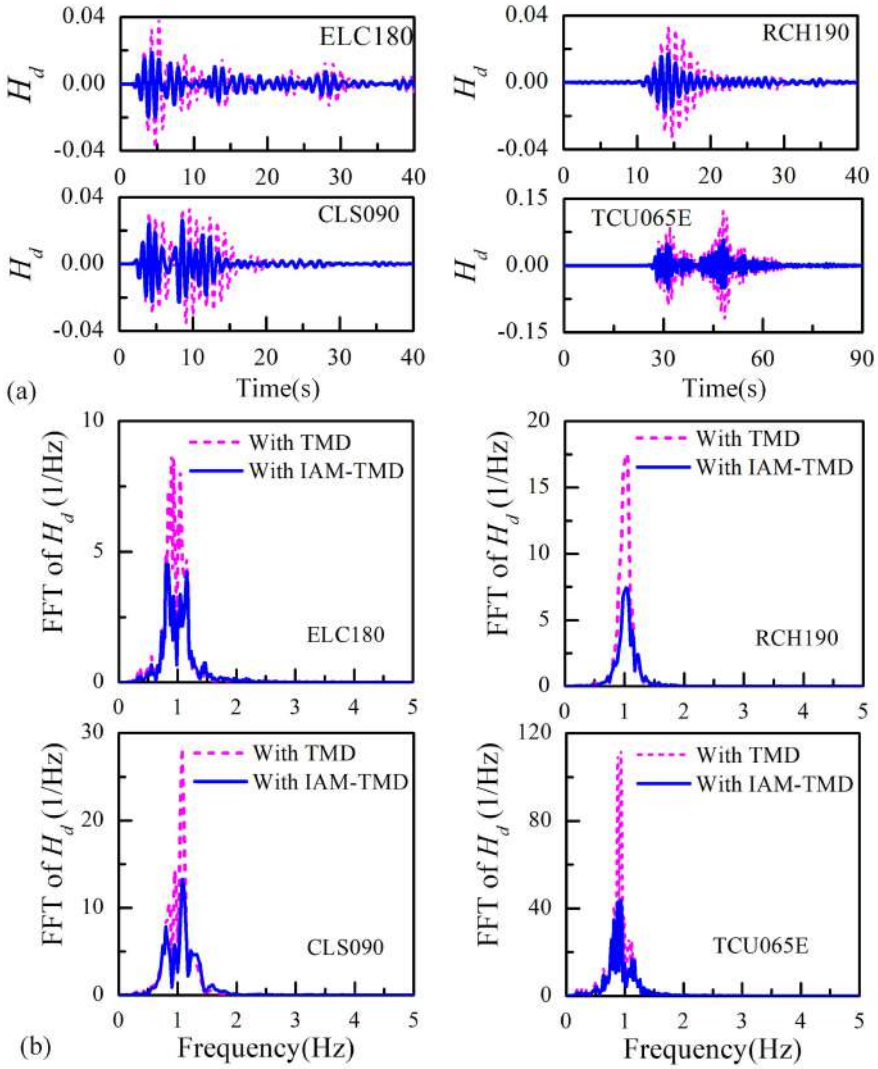

Figure 17: Normalized (a) relative displacement responses of the absorber and (b) their Fourier spectrum with the considered three systems under the different earthquake input.

optimization, it is found that the IAM-TMD can enhance the performance of the TMD when the configurational angle of the IAM is smaller than θ_c. It is found that the H_2 optimization yields larger optimal tuning ratio f_{opt} than H_∞ optimization, especially for cases with a smaller θ and larger α. Conversely, for the damping ratio, the optimal value in the H_2 optimization is smaller than that in the H_∞ optimization, in particular when $\theta < 20^\circ$.

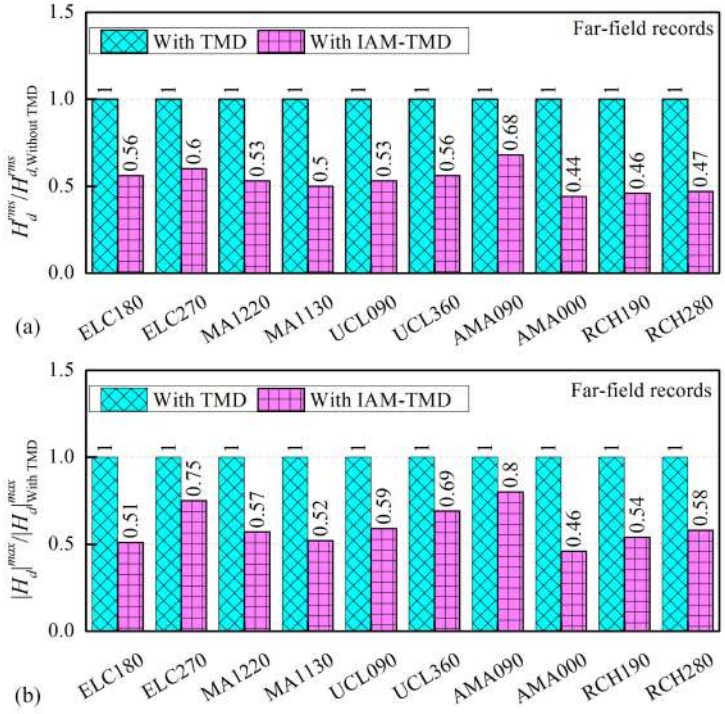

Figure 18: Normalized (a) root mean square and (b) maximum absolute relative displacement responses of the absorber under the considered far-field earthquake inputs.

Numerical simulations confirm that, when TMD is used, displacement responses of the primary structure are suppressed, but the relative displacement responses of the absorber are large. The IAM-TMD instead ensures reduced displacement responses for the primary structure and reduced relative displacement for the absorber, even when the same overall mass is used. Overall, the proposed mechanical amplification system enhances the performance of the TMD effectively.

Future research efforts will be devoted to investigate the applicability of the proposed damper to MDOF systems, the effect of damping on the main structure, as well as the non-linear response of the IAM-TMD system.

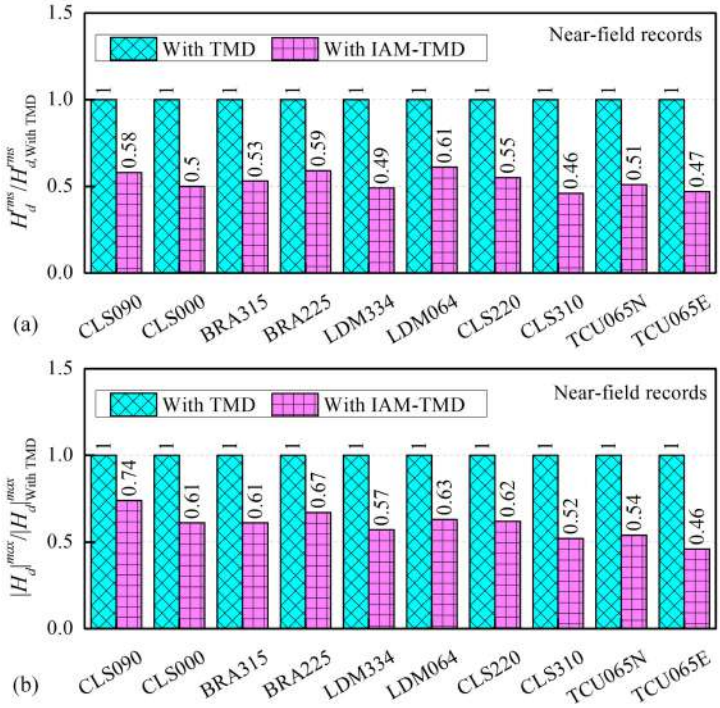

Figure 19: Normalized (a) root mean square value and (b) maximum absolute relative displacement responses of the absorber under the considered near-field earthquake inputs.

Acknowledgement

This work is supported by the National Natural Science Foundation of China (51878031, 51878030) and the Beijing Natural Science Foundation (8182045). The author Zhibao Cheng would like to acknowledge the support of the China Scholarship Council.

Appendix A. Analytical solution for H_2 norm of the considered system

For the stable systems considered here, the transfer function can be given as:

$$\hat{H}_s(s) = \frac{b_{n-1}s^{n-1} + \cdots + b_1 s + b_0}{s^n + a_{n-1}s^{n-1} + \cdots + a_1 s + a_0} \tag{A.1}$$

.

Rewriting it in the controllable canonical form, the minimal state-space realization of $\hat{H}_s(s)$ can be given as [12, 61]:

$$\dot{x} = Ax + Bu, y = Cx \tag{A.2}$$

with,

$$A = \begin{bmatrix} 0 & 1 & 0 & \cdots & 0 \\ 0 & 0 & 1 & \cdots & 0 \\ \vdots & \vdots & \vdots & \ddots & \vdots \\ 0 & 0 & 0 & \cdots & 1 \\ -a_0 & -a_1 & -a_2 & \cdots & -a_{n-1} \end{bmatrix}, \quad B = \begin{bmatrix} 0 \\ 0 \\ \vdots \\ 0 \\ 1 \end{bmatrix}, \quad C = \begin{bmatrix} b_0 \\ b_1 \\ b_2 \\ \vdots \\ b_{n-1} \end{bmatrix}^{\mathrm{T}}. \tag{A.3}$$

The H_2 norm of the stable transfer function $\hat{H}_s(s)$ can be calculated as [12, 61]:

$$|\hat{H}_s(s)|_2^2 = |C(sI - A)^{-1}B| = CLC^{\mathrm{T}}. \tag{A.4}$$

where L is the unique solution of the Lyapunov equation:

$$AL + LA^{\mathrm{T}} + BB^{\mathrm{T}} = 0. \tag{A.5}$$

In particular, the Lyapunov equation Eq. (A.5) can be written as a set of linear algebraic equations with respect to the unknown components of the L matrix. Solving it, the closed-form solution of the L matrix will be obtained. Inserting the solution into Eq. (A.4), the H_2 norm can be obtained [12]:

$$\Phi = F(f)\xi_{id} + \frac{G(f)}{\xi_{id}}. \tag{A.6}$$

Here,

$$F(f) = \frac{(1-2\alpha)(\mu - \alpha\mu + 1)^2[\mu(\alpha\beta - 2\alpha + 1) + 1]}{\mu(\alpha\beta - 2\alpha + 1)^2} f, \tag{A.7}$$

$$G(f) = G_1(f) + G_2(f) + G_3(f) + G_4(f) + G_5(f), \tag{A.8}$$

with

$$G_1(f) = -\frac{1}{4\mu(2\alpha - 1)f}; \tag{A.9}$$

$$G_2(f) = -\frac{(\mu - \alpha\mu + 1)[\mu(\alpha\beta - 2\alpha + 1) + 1]}{2\mu(\alpha\beta - 2\alpha + 1)}; \tag{A.10}$$

$$G_3(f) = -\frac{(\mu - \alpha\mu + 1)^2 f}{4\mu(\alpha\beta - 2\alpha + 1)}; \tag{A.11}$$

$$G_4(f) = -\frac{(2\alpha-1)(\mu-\alpha\mu+1)^2[\mu(\alpha\beta-2\alpha+1)+1]^2 f^3}{4\mu(\alpha\beta-2\alpha+1)^2}; \tag{A.12}$$

$$G_5(f) = \frac{(\mu-\alpha\mu+1)^2[\mu(\alpha\beta-2\alpha+1)+1]f}{4\mu(\alpha\beta-2\alpha+1)}. \tag{A.13}$$

References

[1] H. Frahm, Device for damping vibration bodies, 1909. US Patent No.989/959.

[2] J. Ormondroyd, J. P. Den-Hartog, The theory of the vibration absorber, Transactions of the American Society of Mechanical Engineers 49 (1928) 9–22.

[3] J. P. Den-Hartog, Mechanical Vibration, Mcgraw-Hill Book Company, 3th edition, 1947.

[4] G. B. Warburton, E. O. Ayorinde, Optimum absorber parameters for simple systems, Earthquake Engineering & Structural Dynamics 8 (1980) 197–217.

[5] G. B. Warburton, Optimum absorber parameters for various combinations of response and excitation parameters, Earthquake Engineering & Structural Dynamics 10 (1982) 381 – 401.

[6] L. Zuo, S. Nayfeh, Minimax optimization of multi-degree-of-freedom tuned-mass dampers, Journal of Sound and Vibration 272 (2004) 893 – 908.

[7] L. Zuo, S. A. Nayfeh, The Two-Degree-of-Freedom Tuned-Mass Damper for Suppression of Single-Mode vibration under random and harmonic excitation, Journal of Vibration and Acoustics 128 (2005) 56–65.

[8] G. C. Marano, R. Greco, B. Chiaia, A comparison between different optimization criteria for tuned mass dampers design, Journal of Sound and Vibration 329 (2010) 4880 – 4890.

[9] G. C. Marano, R. Greco, Optimization criteria for tuned mass dampers for structural vibration control under stochastic excitation, Journal of Vibration and Control 17 (2011) 679–688.

[10] A. Sinha, Optimal damped vibration absorber for narrow band random excitations: A mixed h_2 / h_∞ optimization, Probabilistic Engineering Mechanics 24 (2009) 251 – 254.

[11] Y. Hu, M. Z. Chen, Z. Shu, L. Huang, Analysis and optimisation for inerter-based isolators via fixed-point theory and algebraic solution, Journal of Sound and Vibration 346 (2015) 17 – 36.

[12] M. Z. Q. Chen, Y. Hu, Passive Energy Dissipation Systems in Structural Engineering, Science Press, 2019.

[13] T. Asami, O. Nishihara, A. M. Baz, Analytical solutions to h_∞ and h_2 optimization of dynamic vibration absorbers attached to damped linear systems, Journal of Vibration and Acoustics 124 (2002) 284–295.

[14] Y. Cheung, W. Wong, H_2 optimization of a non-traditional dynamic vibration absorber for vibration control of structures under random force excitation, Journal of Sound and Vibration 330 (2011) 1039 – 1044.

[15] Y. Hu, M. Z. Chen, Performance evaluation for inerter-based dynamic vibration absorbers, International Journal of Mechanical Sciences 99 (2015) 297 – 307.

[16] J. R. Sladek, R. E. Klingner, Effect of tuned mass dampers on seismic response, Journal of Structural Engineering 109 (1983) 2004–2009.

[17] P. Lukkunaprasit, A. Wanitkorkul, Inelastic buildings with tuned mass dampers under moderate ground motions from distant earthquakes, Earthquake Engineering & Structural Dynamics 30 (2001) 537–551.

[18] E. Matta, Effectiveness of tuned mass dampers against ground motion pulses, Journal of Structural Engineering 139 (2013) 188–198.

[19] J. Salvi, E. Rizzi, Optimum earthquake-tuned TMDs: Seismic performance and new design concept of balance of split effective modal masses, Soil Dynamics and Earthquake Engineering 101 (2017) 67 – 80.

[20] J. Salvi, E. Rizzi, E. Rustighi, N. S. Ferguson, On the optimization of a hybrid tuned mass damper for impulse loading, Smart Materials and Structures 24 (2015) 085010.

[21] C. Papadimitriou, L. S. Katafygiotis, S.-K. Au, Effects of structural uncertainties on TMD design: A reliability-based approach, Journal of Structural Control 4 (1997) 65–88.

[22] H. Anajafi, R. A. Medina, Robust design of a multi-floor isolation system, Structural Control and Health Monitoring 25 (2018) e2130.

[23] A. Lucchini, R. Greco, G. C. Marano, G. Monti, Robust design of tuned mass damper systems for seismic protection of multistory buildings, Journal of Structural Engineering 140 (2014) A4014009.

[24] J. Salvi, F. Pioldi, E. Rizzi, Optimum tuned mass dampers under seismic soil-structure interaction, Soil Dynamics and Earthquake Engineering 114 (2018) 576 – 597.

[25] M. Abe, T. Igusa, Semi-active dynamic vibration absorbers for controlling transient response, Journal of Sound and Vibration 198 (1996) 547 – 569.

[26] L.-L. Chung, Y.-A. Lai, C.-S. W. Yang, K.-H. Lien, L.-Y. Wu, Semi-active tuned mass dampers with phase control, Journal of Sound and Vibration 332 (2013) 3610 – 3625.

[27] C.-M. Chang, S. Shia, Y.-A. Lai, Seismic design of passive tuned mass damper parameters using active control algorithm, Journal of Sound and Vibration 426 (2018) 150 – 165.

[28] M. C. Smith, Synthesis of mechanical networks: the inerter, IEEE Transactions on Automatic Control 47 (2002) 1648–1662.

[29] M. C. Smith, F.-C. Wang, Performance benefits in passive vehicle suspensions employing inerters, Vehicle System Dynamics 42 (2004) 235–257.

[30] F.-C. Wang, M.-K. Liao, B.-H. Liao, W.-J. Su, H.-A. Chan, The performance improvements of train suspension systems with mechanical networks employing inerters, Vehicle System Dynamics 47 (2009) 805–830.

[31] F.-C. Wang, M.-R. Hsieh, H.-J. Chen, Stability and performance analysis of a full-train system with inerters, Vehicle System Dynamics 50 (2012) 545–571.

[32] Y. Hu, M. Z. Chen, Y. Sun, Comfort-oriented vehicle suspension design with skyhook inerter configuration, Journal of Sound and Vibration 405 (2017) 34 – 47.

[33] Y. Hu, K. Wang, Y. Chen, M. Z. Chen, Inerter-based semi-active suspensions with low-order mechanical admittance via network synthesis, Transactions of the Institute of Measurement and Control 40 (2018) 4233–4245.

[34] P. Brzeski, T. Kapitaniak, P. Perlikowski, Novel type of tuned mass damper with inerter which enables changes of inertance, Journal of Sound and Vibration 349 (2015) 56 – 66.

[35] P. Brzeski, M. Lazarek, P. Perlikowski, Experimental study of the novel tuned mass damper with inerter which enables changes of inertance, Journal of Sound and Vibration 404 (2017) 47 – 57.

[36] F.-C. Wang, C.-W. Chen, M.-K. Liao, M.-F. Hong, Performance analyses of building suspension control with inerters, in: 2007 46th IEEE Conference on Decision and Control, pp. 3786–3791.

[37] F.-C. Wang, M.-F. Hong, C.-W. Chen, Building suspensions with inerters, Proceedings of the Institution of Mechanical Engineers, Part C: Journal of Mechanical Engineering Science 224 (2010) 1605–1616.

[38] K. Ikago, K. Saito, N. Inoue, Seismic control of single-degree-of-freedom structure using tuned viscous mass damper, Earthquake Engineering & Structural Dynamics 41 (2012) 453–474.

[39] I. F. Lazar, S. Neild, D. Wagg, Using an inerter-based device for structural vibration suppression, Earthquake Engineering & Structural Dynamics 43 (2014) 1129–1147.

[40] L. Marian, A. Giaralis, Optimal design of a novel tuned mass damper inerter (TMDI) passive vibration control configuration for stochastically support-excited structural systems, Probabilistic Engineering Mechanics 38 (2014) 156 – 164.

[41] A. Giaralis, F. Petrini, Wind-induced vibration mitigation in tall buildings using the Tuned Mass-Damper-Inerter, Journal of Structural Engineering 143 (2017) 04017127.

[42] A. Giaralis, A. Taflanidis, Optimal tuned mass-damper-inerter (TMDI) design for seismically excited MDOF structures with model uncertainties based on reliability criteria, Structural Control and Health Monitoring 25 (2018) 2082.

[43] D. D. Domenico, G. Ricciardi, An enhanced base isolation system equipped with optimal tuned mass damper inerter (TMDI), Earthquake Engineering & Structural Dynamics 47 (2018) 1169–1192.

[44] D. D. Domenico, P. Deastra, G. Ricciardi, N. D. Sims, D. J. Wagg, Novel fluid inerter based tuned mass dampers for optimised structural control of base-isolated buildings, Journal of the Franklin Institute (2018).

[45] K. Xu, K. Bi, Q. Han, X. Li, X. Du, Using tuned mass damper inerter to mitigate vortex-induced vibration of long-span bridges: Analytical study, Engineering Structures 182 (2019) 101 – 111.

[46] R. Ma, K. Bi, H. Hao, Mitigation of heave response of semi-submersible platform (ssp) using tuned heave plate inerter (THPI), Engineering Structures 177 (2018) 357 – 373.

[47] L. Lu, Y.-F. Duan, B. F. Spencer Jr, X. Lu, Y. Zhou, Inertial mass damper for mitigating cable vibration, Structural Control and Health Monitoring 24 (2017) e1986.

[48] R. Zhang, Z. Zhao, K. Dai, Seismic response mitigation of a wind turbine tower using a tuned parallel inerter mass system, Engineering Structures 180 (2019) 29 – 39.

[49] Z. Zhao, R. Zhang, Y. Jiang, C. Pan, Seismic response mitigation of structures with a friction pendulum inerter system, Engineering Structures 193 (2019) 110 – 120.

[50] Z. F. Shi, Z. B. Cheng, H. J. Xiang, Periodic Structures: Theory and Applications to Seismic Isolation and Vibration Reduction, Science Press, 2017.

[51] Z. Cheng, Z. Shi, Novel composite periodic structures with attenuation zones, Engineering Structures 56 (2013) 1271–1282.

[52] M. Li, Z. Cheng, G. Jia, Z. Shi, Dimension reduction and surrogate based topology optimization of periodic structures, Composite Structures 229 (2019) 111385.

[53] X. Wang, H. Liu, Y. Chen, P. Gao, Beneficial stiffness design of a high-static-low-dynamic-stiffness vibration isolator based on static and dynamic analysis, International Journal of Mechanical Sciences 142-143 (2018) 235 – 244.

[54] X. Feng, X. Jing, Z. Xu, Y. Guo, Bio-inspired anti-vibration with nonlinear inertia coupling, Mechanical Systems and Signal Processing 124 (2019) 562 – 595.

[55] X. Feng, X. Jing, Human body inspired vibration isolation: Beneficial nonlinear stiffness, nonlinear damping & nonlinear inertia, Mechanical Systems and Signal Processing 117 (2019) 786 – 812.

[56] C. Yilmaz, G. M. Hulbert, N. Kikuchi, Phononic band gaps induced by inertial amplification in periodic media, Physical Review B 76 (2007) 054309.

[57] C. Yilmaz, G. Hulbert, Theory of phononic gaps induced by inertial amplification in finite structures, Physics Letters A 374 (2010) 3576 – 3584.

[58] N. M. M. Frandsen, O. R. Bilal, J. S. Jensen, M. I. Hussein, Inertial amplification of continuous structures: Large band gaps from small masses, Journal of Applied Physics 119 (2016) 124902.

[59] X. Li, M. Guo, S. Dong, A flex-compressive-mode piezoelectric transducer for mechanical vibration/strain energy harvesting, IEEE Transactions on Ultrasonics, Ferroelectrics, and Frequency Control 58 (2011) 698–703.

[60] X. Wang, Z. Shi, J. Wang, H. Xiang, A stack-based flex-compressive piezoelectric energy harvesting cell for large quasi-static loads, Smart Materials and Structures 25 (2016) 055005.

[61] J. C. Doyle, B. A. Francis, Feedback Control Theory, Oxford: Maxwell Macmillan Int, 1992.